J. Dandois
(Onera)
P.-Y. Pamart
(Snecma)

E-mail: julien.dandois@onera.fr

NARX Modeling and Extremum-Seeking Control of a Separation

A numerical study concerning a SISO active closed-loop separation control on a rounded step is presented. A first study of the synthetic jet frequency effect on the separation shows that the mean separation bubble surface is minimized if the mean pressure of a single wall pressure sensor is maximized. With the aim of designing a closed-loop strategy for the control of the recirculation bubble, a NARX black-box model of the pressure signal is identified using a single unsteady RANS simulation. The basic extremum-seeking algorithm is improved with an adaptive gain, to guarantee algorithm performance and this modification is validated against the nonlinear black-box model of the forced flow. Then, the robust adaptive closed-loop is applied in real-time with an unsteady RANS simulation. Closed-loop results show the ability of the extremum-seeking control with adaptive gain to automatically control the separation, by minimizing the recirculation bubble surface using an unsteady RANS simulation.

Introduction

Separated flows occur in a variety of engineering applications and generally have a negative impact on performance. Recently, numerous attempts have been made to control turbulent separated flows, in order to improve aerodynamic performance. Even though open-loop control has been successful in suppressing separation, it often results in large requested mass flow rate values, which are not realistic for practical use on a real aircraft. More advanced closed-loop active flow control techniques are seen as a promising way to reduce the control cost, using a real-time adaptation of flow perturbations. The closed-loop control is generally performed on the mass flow rate for continuous or pulsed blowing and, in the case of separation control by synthetic jets, on the voltage amplitude. The relation between the aerodynamic gain and the mass flow rate or the voltage amplitude is generally monotonic, with some saturation (see for example [29]).

On the contrary, the relation between the aerodynamic gain and the forcing frequency sometimes exhibits an optimum frequency (see [30]), which allows the required energy input in the system to be reduced. The application of active flow control in a practical case requires a self-sustaining, autonomous control system to adapt the forcing frequency to the freestream velocity, for example.

When the actuator-sensor relationship is linear, the actuation and sensor signals can be linked by a transfer function and all of the linear controller theory of the automatics domain can be used, for instance: robust control, predictive control and adaptive control. On the contrary, when the actuator-sensor relationship is characterized by a steady-state map with an extremum, model-independent controllers based on gradient methods can be used. The extremum-seeking algorithm is especially well suited in this case. It is a non-model-based method for the control of non-linear plants, characterized by an output extremum in the steady state (Ariyur & Krstic [2] and Krstic & Wang [21]). This control technique has been used in different studies: Banaszuk et al. [3] and King et al. [20] used it to recover the pressure in a separated diffuser flow. Extremum-seeking and its variant, slope-seeking, were experimentally tested by Becker et al. [5-6] for separation control on a NACA 4412 flap. Pastoor et al. [26] applied it to control the separation behind a D-shaped body and Beaudoin et al. [4] to control the bluff-body drag. In order to improve the seeking algorithm, Henning et al. [18] added some slope estimators.

This short review shows the efficiency of the extremum-seeking strategy to control separation and underlines the fact that this strategy was only applied in experiments. A feature brought by our study is the fact that it is entirely numerical. It adds the challenge that the closed-loop convergence time must be lower than few seconds, in order to be compatible with actual computer capacities. Due to this computational cost, unsteady RANS (URANS) simulations are preferred to large-eddy simulations.

This study is devoted to the closed-loop control of a rounded step separation by synthetic jet, where the only real-time optimized

parameter is the frequency. The pressure of a single wall sensor in the separated zone is the output of the closed-loop. Since the steady-state map in the frequency domain exhibits an optimum frequency, the extremum-seeking algorithm is used with some improvements to increase convergence rate.

First, in order to tune the extremum-seeking parameters and validate the closed-loop strategy before applying it in a URANS computation, a reduced-order model is required to be able to quickly test the effect of all parameters. In order to have a model offering a good compromise between simplicity, cost and accuracy, a Nonlinear Auto-Regressive with eXogenous input (NARX model) has been selected.

This paper is divided into three main parts. In the first part, the NARX model is presented. In the second one, the model is identified and validated. Unsteady Reynolds-Averaged Navier-Stokes (URANS) computations are performed to obtain the unsteady flow response to the synthetic jet actuation. The location of the pressure sensor is justified and the relationship between the pressure information and the separation bubble geometry is evidenced. In a second step, the structure of the NARX model is chosen. A rigorous methodology is then developed to justify the choice of each of these model parameters and both the dynamic and the steady state responses of the model are assessed. The proposed methodology is inspired by the one developed by Box and Jenkins [7] for linear ARMAX models. The choice of the polynomial power, which introduces the nonlinearity, is specific to this study. In the third part, the extremum-seeking algorithm is presented, as well as its improvements: the adaptive gain and the use of Bessel filters. Then, the closed-loop is applied to the NARX model to check the convergence time before being applied in an URANS simulation.

Black-box modeling

Due to the nature of the governing equation, a nonlinear model is studied. Nevertheless, its accuracy will be compared to a linear model for each application, to justify the gain brought by the nonlinear modeling. The idea is not to capture the flow physics, but rather only to represent the pressure output as a function of the forcing signal. This is the reason why a black-box model is used. The NARMAX model [9] is a class of model that links inputs u and outputs y with nonlinear relationships. Its general formulation is written in equation (1), where G denotes a nonlinear function, k is the discrete time, n_u and n_y are the number of past inputs and past outputs, respectively, and ε and ξ stand for possible noise and residual error.

$$y(k) = G(y(k-1),...,y(k-n_y),u(k-1),...,$$
$$,u(k-n_u),\varepsilon(k-1),...,\varepsilon(k-n_y)) + \xi(x_k) \quad (1)$$

The nonlinear function G can be a polynomial, a neural network, a wavelet network, or any other nonlinear function.

In this study a polynomial NARX (a NARMAX with the noise terms excluded, see Section "Model identification and validation" below for the justification) is computed. The advantage of the polynomial NARX model is that the model is linear with respect to the coefficients of the model θ. The specific model structure used is described in equation (2).

$$y(k) = \theta_0 + \sum_{i=1}^{p}\sum_{j=1}^{n_y}\theta_{y|i,j}y(k-j)^i + \sum_{i=1}^{p}\sum_{j=1}^{n_u}\theta_{u|i,j}u(k-j-lag_u)^i$$
$$+ \sum_{i=1}^{n_y}\sum_{j=1}^{n_y}\theta_{yy|i,j}y(k-i)y(k-j) \quad (2)$$
$$+ \sum_{i=1}^{n_u}\sum_{j=1}^{n_u}\theta_{uu|i,j}u(k-i-lag_u)u(k-j-lag_u)$$

where the θ_{ij} are the coefficients of the model, p is the polynomial power and lag_u is the delay between the output and the input, to take into account, for example, the convection time of the vortices between the actuator location and the sensor. The cross-terms $u(k-i) \times y(k-j)$, as well as the terms of order over 2 on the input u or the output y, are not taken into account in the model, in order to keep a reasonable total number of terms and avoid the problems of overfitting. Moreover, it must be noticed that the constant term θ_0 is particularly important, since it has been observed that it enables the mean output to be different from zero. Therefore, it allows the model to reproduce the static map $<P> = f(F^+)$, where $<P>$ is the time-averaged wall pressure, F^+ is the reduced frequency defined by $F+ = f L_{UC} / U_\infty$ and L_{UC} is the separation length of the uncontrolled case.

The total number of regressors is:

$$n_\theta = 1 + p(n_u + n_y) + n_y(n_y-1)/2 + n_u(n_u-1)/2 \quad (3)$$

and corresponds to the number of coefficients θ to be determined (see Section "Model identification and validation").

The identification phase consists in computing the NARX regressors θ. For this purpose, an identification signal u must be defined to explore the system response to an actuation. In this study, a periodic forcing is considered. In order to model the flow response, the identification signal must randomly explore the entire frequency range of interest. Then, the resulting model is not expected to be valid out of this frequency range.

Let Y_M be the URANS identification simulation pressure output vector, Θ be the regressor vector, M be the NARX relation matrix between Y_M and Θ so that $M\Theta = Y_M$, with the property that:

$$Y_M^T = (y(k), y(k-1),..., y(k-n_k)) \quad (4)$$

and

$$\Theta^T = (\theta_0, \theta_1,..., \theta_{n_\theta}) \quad (5)$$

where n_k is the number of samples, which must be larger than the number of regressors n_θ.

Since the number of measurements is larger than the number of regressors, the problem is overdetermined. The standard approach to solve an overdetermined system of linear equations given as $M\Theta = Y_M$ is known as linear least squares and seeks to minimize the residual $\left\|M\Theta - Y_M\right\|^2$, where $\|.\|$ is the Euclidean norm.

The matrix M is generally ill-conditioned. The Tikhonov regularization [32] is the most commonly used regularization method for ill-posed problems. In order to give preference to a particular solution

with desirable properties, the regularization term is included in this minimization: $\left\| M\Theta - Y_M \right\|^2 + \left\| \Gamma\Theta \right\|^2$ for some suitably chosen Tikhonov matrix Γ. In many cases, this matrix is chosen as the identity matrix $\Gamma = I$, giving preference to solutions with the smallest norm. In other cases, high-pass operators (e.g., a difference operator or a weighted Fourier operator) may be used to enforce smoothness, if the underlying vector is believed to be mostly continuous. This regularization improves the conditioning of the problem, thus enabling the existence of a numerical solution. An explicit solution, denoted by $\hat{\Theta}$, is given by:

$$\hat{\Theta} = (M^T M + \Gamma^T \Gamma)^{-1} M^T Y_M \qquad (6)$$

The effect of regularization may be varied via the scale of matrix Γ (e.g. $\Gamma = \alpha I$). For $\alpha = 0$, this is reduced to the non-regularized least squares solution, provided that $(M^T M)^{-1}$ exists.

Separation control by a synthetic jet slot over a rounded ramp

Configuration

The geometry of the configuration is displayed in figure 1. The ramp height h is equal to 20 mm and the maximum slope is equal to 35°. The shape of the rounded backward-facing step is given by equation:

$$\frac{y}{h} = \frac{1}{2\pi}\left(\sin\left(\frac{a\pi x}{h}\right) - \frac{a\pi x}{h}\right)$$

where $\frac{x}{h} \in \left[0; \frac{2}{a}\right]$ and $\alpha = 0.703$.

The shape is the same as the one defined in Dandois et al. [11]. The Mach number M_∞ is set equal to 0.31 and the free-stream velocity U_∞ is equal to 104.0 m.s^{-1}.
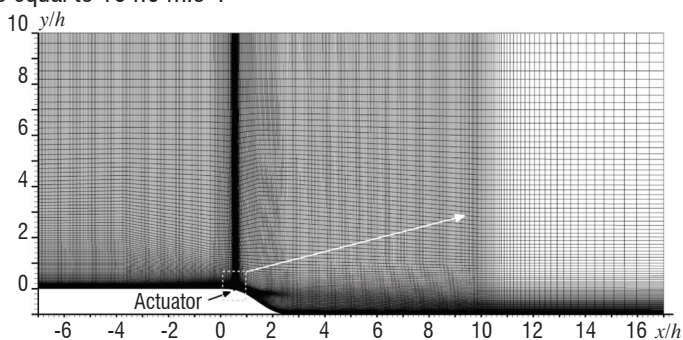

Figure 1- Flow configuration with the synthetic jet cavity and grid

The boundary layer thickness at $x/h = -1$ and its momentum thickness are equal to $0.5h$ and $0.05h$, respectively. The Reynolds number Re_θ based on the momentum thickness is equal to 1,460. The Reynolds number Re_h, based on the ramp height and freestream velocity, is equal to 29,200. The synthetic jet orifice consists in a two-dimensional slot. Its windward edge is located close to the mean separation point of the uncontrolled flow, following the methodology proposed by Neumann and Wengle [23].

The coordinate system is the following: x is oriented in the streamwise direction, y is vertical and z is in the spanwise direction. The origin is located at the beginning of the ramp.

Actuator

The actuator is composed of a slot cavity and described by four parameters: slot width d, slot height H_s, cavity width W_c and cavity height H_c. The actuator dimensions used in these computations are $d = 0.55$ mm, $H_s = d$, $W_c = 2d$ and $Hc = d/2$ (figure 2).
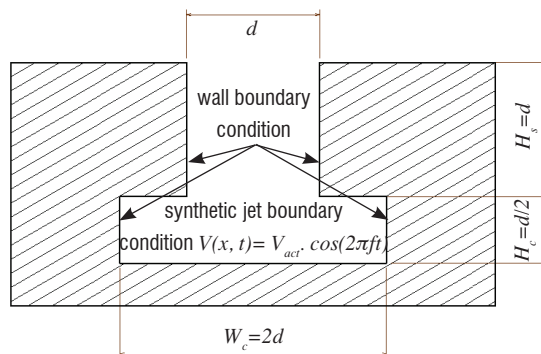

Figure 2 - Actuator geometry

The reduced frequency work range is chosen within the interval $F^+ \in [0.1;10]$. Quantitatively, $F^+ = 1$ corresponds to $f = 911$ Hz.

Actuator dimensions have been calculated with respect to classical synthetic jet designing criteria: the synthetic jet formation criterion and a minimal value of the Stokes number (Holman et al. [19] and Schuster et al. [28]). The resonance frequency definition of Gallas et al. [13,14] has been used to set up cavity design, with a resonance frequency chosen at $F^+_{resonance} \approx 59$, which is far enough from $F^+_{max} = 10$ to avoid resonance effects at high frequency. The synthetic jet forcing amplitude is characterized by its momentum coefficient, which is defined by:

$$C_\mu = \frac{\rho_j d V_{RMS}^2}{\rho_\infty L_{UC} U_\infty^2} \qquad (7)$$

where ρ_j is the synthetic jet density, V_{RMS} is the root-mean-square value of the synthetic jet velocity at the orifice exit and ρ_∞ is the freestream density.

Numerical method

The geometry, the grid and the numerical method are the same as those used in [15] to compare the URANS and LES techniques.

The FLU3M code is a finite volume solver for the compressible Navier Stokes equations. The turbulence model used for URANS simulations is the Spalart-Allmaras one [31] with the rotation correction of Daclès-Mariani et al. [10]. The time integration is carried out by means of the second-order-accurate backward scheme of Gear [16]. The time step is equal to 5.10^{-7} s.

The spatial scheme is the one proposed by Mary and Sagaut [22] which is second-order-accurate. The accuracy of the solver has been assessed in various applications at Onera [11, 12, 25, 27, 33].

The streamwise length of the computation domain is $24h$ ($7.5h$ upstream of the separation point and $12h$ downstream from the reattachment point of the uncontrolled case), its height is $10h$ in the inflow plane. The grid is composed of 66,265 cells distributed as 515×127 for the ramp, 10×38 for the slot and 20×24 for the cavity.

Grid spacings in the streamwise and in the wall-normal directions are $\Delta x^+ = 50$ and $\Delta z^+_{min} = 0.5$, respectively. A view of the URANS grid in the x-z plane is displayed in figure 1.

Each controlled case is initialized with the same field. A transient time equivalent to 4.5 flow-through times was necessary to reach the permanent regime. Then, 11 flow-through times were found sufficient to obtain converged statistics.

To simulate the diaphragm displacement, a blowing/suction condition with a top-hat spatial distribution and sinusoidal temporal variation is implemented on the entire cavity bottom surface (figure 2): $V(x,t) = V_{act}. \cos(2\pi f t)$. Previous studies have shown that the computation of the whole actuator cavity was mandatory for an accurate description of the synthetic jet effect on the separation.

Open-loop results

This section outlines some open-loop results regarding the forcing frequency effect, useful to determine a closed-loop strategy. It has two purposes. The first objective of this open-loop study is to find a criterion to quantify the control effect on the separation. The second one is to justify the use of a local measurement (which will be the model single output) by correlating it with the previous criterion.

Uncontrolled flow

The mean separation bubble contour results from the calculation at each abscissa of the integral of the mass flux in the wall normal direction. The zero-mass-flux line gives the separation bubble contour from which the bubble surface is deduced. This line and streamlines for the uncontrolled flow case are given in figure 3. From the skin friction distribution (not shown), it is found that the separation point is located at $x/h = 0.53$ and the reattachment point at $x/h = 6.26$, so the separation length is $L_{UC}/h = 5.73$.
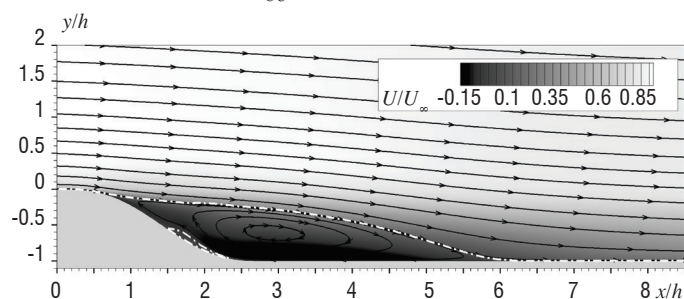

Figure 3 - Uncontrolled flow: streamwise non-dimensional velocity with streamlines and zero mass-flux line (dash-dot line)

Open-loop controlled cases

URANS computation series were performed in order to study the forcing frequency effect with $V_{act} = 39.9$ m.s^{-1}. This velocity corresponds to a theoretical momentum coefficient $C\mu$ equal to 0.28 %.

As a reminder, the reduced frequency is defined by $F^+ = f.L_{uc}/U_\infty$. The Strouhal number used in this paper is based on the ramp height: $St = f.h/U_\infty$.

The reduced frequency work range is chosen within the interval $F^+ \in [0.1; 10]$, in which 23 computations have been carried out. The set of reduced frequency forcing cases is: $F^+ = \{0.1; 0.3; 0.4;$

0.5; 0.7; 0.9; 0.95; 1.0; 1.05; 1.055; 1.06; 1.065; 1.07; 1.075; 1.1; 1.2; 1.5; 2.0; 2.5; 3.0; 4.0; 6.0; 10.0}.

Forcing results on the mean bubble surface reduction

This study is based on URANS computations to make its computational cost acceptable. It is subject to classical RANS limitations; in particular, the results are not free from model sensitivity (see in particular the turbulence model study on this geometry in [15]). Nevertheless, we only need frequency sensitivity results to validate our closed-loop strategy. A previous LES study of synthetic jet frequency and amplitude effects in open-loop brings more physical meaning to the assessment of different control criteria (see Pamart et al. [24]).

For some frequencies, the forcing by the synthetic jet significantly modifies the entire flow. Consequently, some flow parameters are modified, such as pressure and viscous drag, mean separation and reattachment locations, mean recirculation bubble shape, turbulence level, etc. The mean recirculation bubble surface S, non-dimensionalized by the baseline separation bubble surface S_0, is plotted as a function of the forcing frequency in figure 4. The separation surface decreases with the reduced frequency for $0.1 \leq F^+ \leq 0.7$. The separation bubble surface is a minimum for F^+ around 0.7. For this reduced frequency, the bubble surface is reduced by 70 %. Then, for $0.7 \leq F^+ \leq 2$, the separation surface increases with the reduced frequency. For, $F^+ \geq 2$, there is no longer any effect of the control on the separation surface, since S/S_0 remains nearly equal to 1.
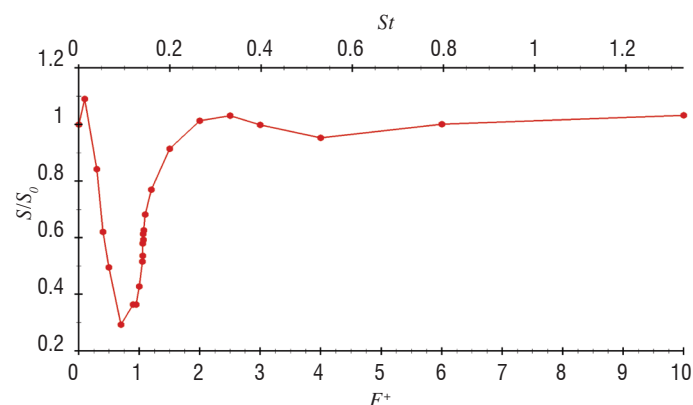

Figure 4 - Forcing frequency effect on the nondimensionalized mean separation bubble surface

Criterion and input choice for the closed-loop

In order to reduce the recirculation bubble surface, the closed-loop algorithm needs a measure of this criterion. The measurement of the bubble surface is not practically feasible, but the idea is to correlate this bubble surface with a wall pressure sensor. By comparing figures 4 and 5, one can observe that, in this case, a decrease of the separation bubble surface is concomitant with an increase of the wall pressure in the separated zone. Thus, the objective of the closed-loop could be to maximize the wall pressure at a given location.

The time-averaged wall pressure from the 23 URANS computations is plotted in figure 5, as a function of the forcing frequency and the x-coordinate. The mean pressure maximum corresponding to the optimal reduced frequency is extracted from this figure and the evolution of this optimal frequency is plotted in figure 6, as function of the x-coordinate. For $2.3 \leq x/h \leq 3.8$, the maximum mean pressure is obtained for a reduced frequency equal to 0.7, which exactly corresponds

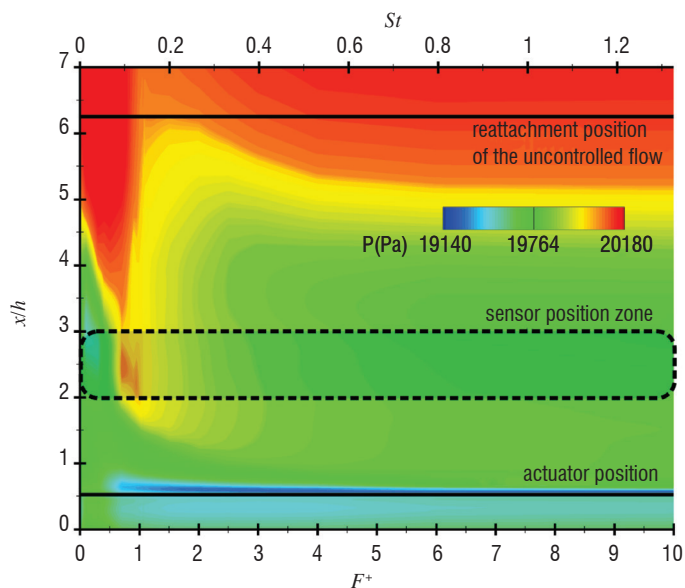to the reduced frequency for which the recirculation bubble surface is minimum in figure 4.

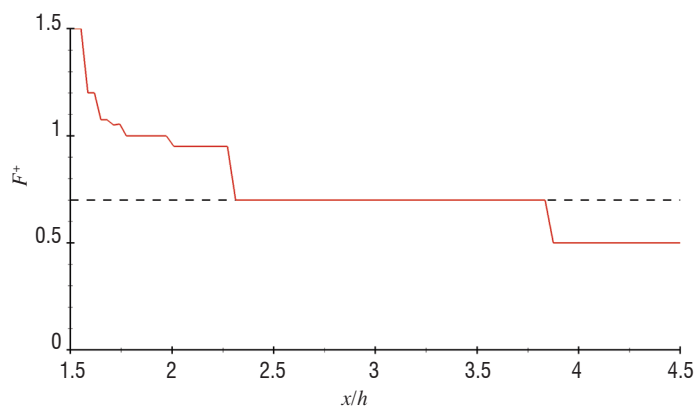Figure 5 - Mean wall pressure as function of forcing frequency and x-coordinate

Figure 6 - Sensor position effect on the reduced frequency corresponding to the mean pressure maximum
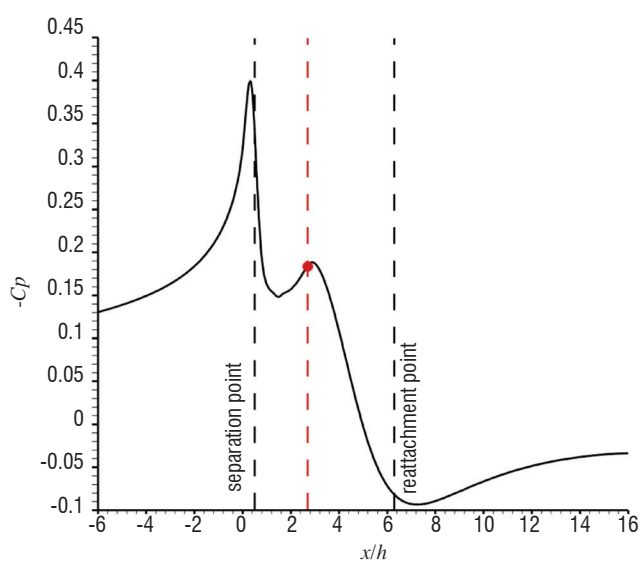

Figure 7 - Wall pressure distribution of the baseline (uncontrolled), showing the pressure sensor location (red dot)

Finally, the wall pressure sensor is chosen at $x/h = 2.71$, near the middle of the separated zone (figure 7). For example, the control objective could be to maximize the pressure at this location. A closed-loop algorithm, such as the extremum-seeking algorithm, is especially well suited for this purpose.

In the following, the objective will be to identify a model that links the actuator output velocity with the wall pressure sensor at $x/h = 2.71$.

Model identification

Identification signal

Due to the computational cost of URANS simulations, we cannot afford to collect a time signal of several seconds with a time step of 5.10^{-7} s. However, it is useful to consider that for $F^+ \geq 3$, the forcing effect on the flow is negligible (see figure 4 again). A NARX black-box model is then identified on a reduced frequency range $F^+ \in [0.1; 3]$, which is divided in 30 steps. Moreover, a good representation of the process steady-state map is made accessible if the signal is compounded of some command plateaus, which allow the flow to converge towards a steady state. With these two ingredients, the signal shape consists in a series of sinusoids of equal length. Each frequency is different and randomly distributed over the frequency range.

The duration of every command step is set equal to 29.4 ms (roughly twice the transient time), which results in a total signal duration of 0.9 s. In order to smooth the discontinuities generated by the steps, the signal is filtered by a first order transfer function, with a time constant equal to 0.35 ms. The reduced frequencies F^+ used for the identification are given in figure 8. The sinusoidal signal with the frequencies of figure 8 is then imposed as a boundary condition on the cavity bottom wall. The momentum coefficient C_μ is constant and equal to 0.28 %. The signal sampling is chosen such that the highest frequency is discretized by at least 12 samples. Consequently, the time step used for the NARX model is $2.5 \ 10^{-5}$ s.
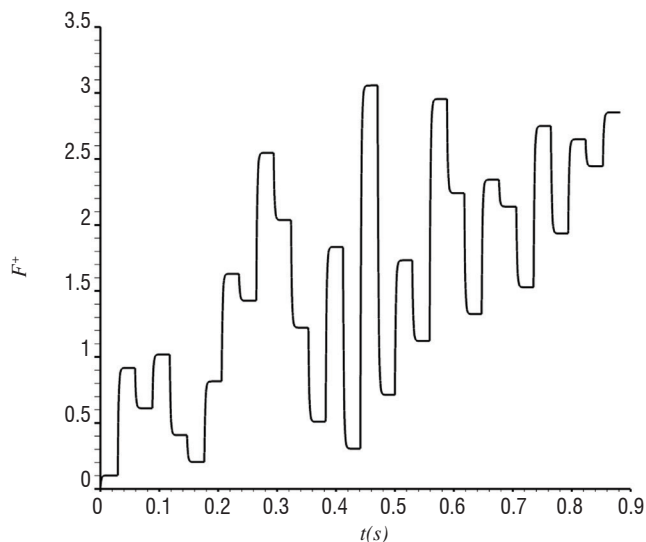

Figure 8 - Input sequence of reduced frequency for the NARX identification

Model identification and validation

A URANS simulation enables us to obtain the response of the considered pressure sensor to the identification signal. The model time

step being already fixed, the NARX parameters to set are the number of past elements for each NARX term (n_y, n_u), the polynomial power p and the lag lag_u. The lag lag_u and the number of past inputs n_u are found using the intercorrelation between the forcing u and the pressure y (figure 9). It can be seen that the intercorrelation is maximum for $lag = 46$. In this figure, the lag values for which the intercorrelation is higher than a predefined user threshold (±0.02) are picked up (red part of the curve with dots), since it means that these output terms are correlated with the input. lag_u is the first abscissa for which the intercorrelation is larger than the threshold ($lag_u = 2$). n_u is the difference between the abscissa above which the intercorrelation falls definitely below the threshold level (here $lag = 113$) and lag_u. Thus, in order to take into account the most correlated terms in the model, lag_u is chosen equal to 2 and $n_u = 111$.
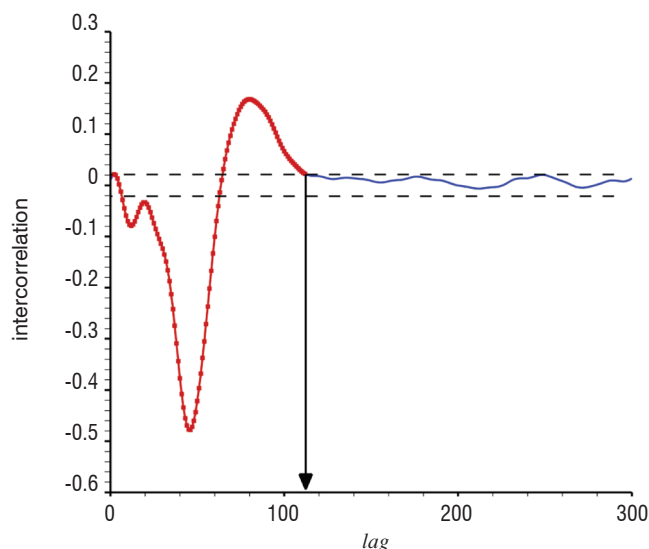
Figure 9 - Intercorrelation between the pressure y and the forcing u, for different lag values of u
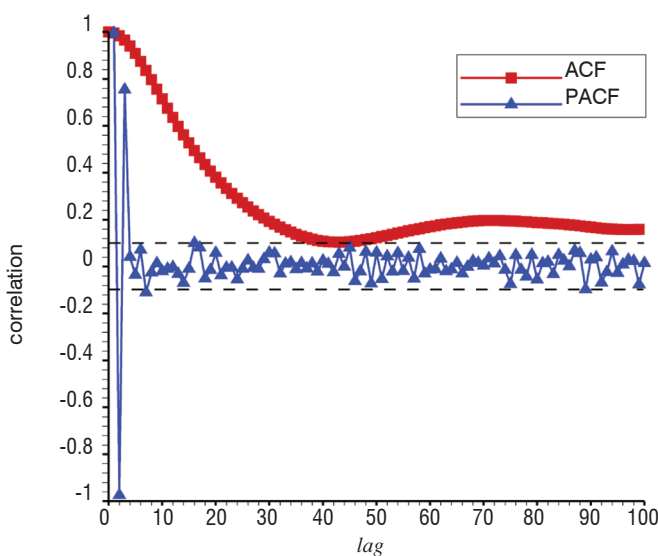
Figure 10 - Autocorrelation function (in red, square symbols) and partial autocorrelation function (in blue, triangle symbols) of the output y

Concerning the value of n_y, the partial autocorrelation function on the output y is computed (figure 10) as recommended by Box & Jenkins [7], to find the order m of an Auto-Regressive Model $AR(m)$. The partial autocorrelation of an $AR(m)$ process becomes zero at lag

$m + 1$ and greater, so the partial autocorrelation function is examined to see if there is evidence of a departure from zero. This is usually determined by placing a 95 % confidence interval on the sample partial autocorrelation plot (black dashed line). Figure 10 shows that the autocorrelation function (ACF) decreases gradually, whereas the partial autocorrelation function (PACF) is close to zero for $n_y > 3$, which means that an $AR(2)$ model should be used. Consequently, n_y is chosen equal to 3.

The autocorrelation function of a $MA(q)$ process becomes zero at lag $q + 1$ and greater. Since the ACF tails off gradually and does not cut off after n_y lags, a Moving Average $MA(q)$ model should not be considered here (see Box & Jenkins [7]); thus, a NARX structure (without noise ε) is chosen, which justifies the fact that the noise terms were excluded in equation (2).

A parametric study of the effect of the model power p is then performed for a fixed value of the Tikhonov regularization coefficient $\alpha = 2$. This value of the regularization coefficient is chosen following the L-$curve$ rule (see figure 11 and Hansen [17]): the optimum value of α is obtained when the L-$curve$ is the closest to the axis origin.
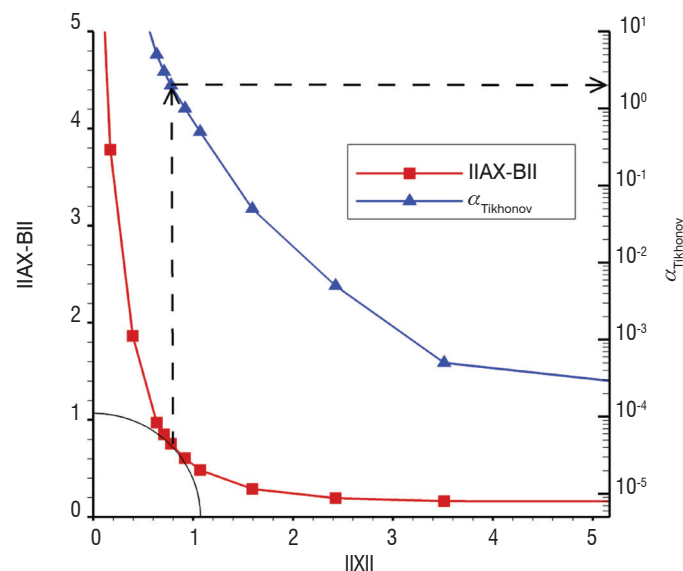

Figure 11 - L-$curve$ of the chosen NARX model

The range of the p parameter studied is $p \in [3; 7]$ (figure 12). The model power p is chosen to minimize the Akaike Information Criterion (AIC) (see [1]) and its modified definition ($AICc$), which increases the weight of the number of regressors n_θ when it becomes large which is the case here. They are defined by:

$$AIC = -2\ln(L) + 2n_\theta$$

$$AICc = AIC + \frac{2n_\theta(n_\theta + 1)}{n - n_\theta - 1}$$

(8)

where L is the likelihood function of the model, n_θ is the total number of regressors and n is the number of samples. If the error between the model output y_m and the learning data y is assumed to be zero-mean Gaussian (it has been checked that it is true here), the previous expression of the AIC criterion becomes (see [8]):

$$AIC = n\ln(RSS / n) + 2n_\theta$$

(9)

where RSS is the residual sum of squares:

$$RSS = \sum_{i=1}^{n_k} (y_m(i) - y(i))^2$$

This criterion is the sum of two terms: the first one depends on the error between the model and the true measurement and the second one includes a penalty, which increases with the number of regressors in the model. This prevents overfitting. The objective is to minimize one of these two criteria.

Figure 12 shows that the AIC of the model is minimized for $p = 6$ and that the $AICc$ is minimized for $p = 5$. Since AICc has a larger penalty on the number of regressors, we choose $p = 5$.
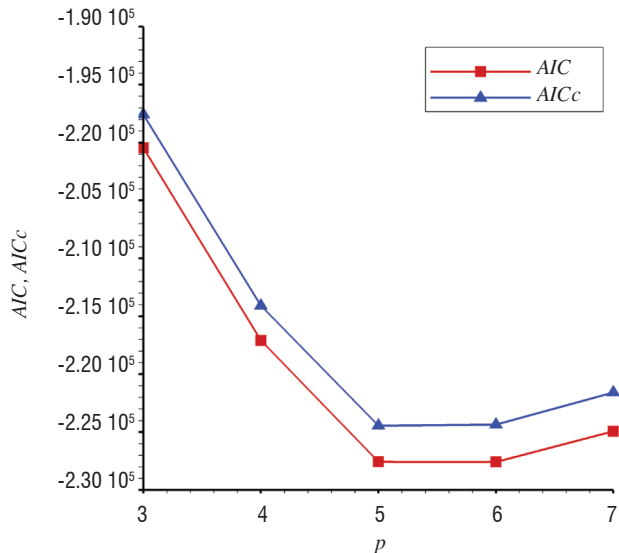
Figure 12 - *AIC & AICc criteria as a function of the NARX model power p.*

To assess the performance of the NARX model, a fit coefficient (which must be maximized) is defined by equation (10). In this coefficient, the mean squared prediction error (MSPE) between the identification signal y and the NARX model y_m is computed

$$fit = 100 \times \left(1 - \sqrt{\frac{\sum_{i=1}^{n_k}(y_m(i)-y(i))^2}{\sum_{i=1}^{n_k}(y(i)-\overline{y}(i))^2}} \right) \qquad (10)$$

where $\overline{y}$ is the mean value of y.
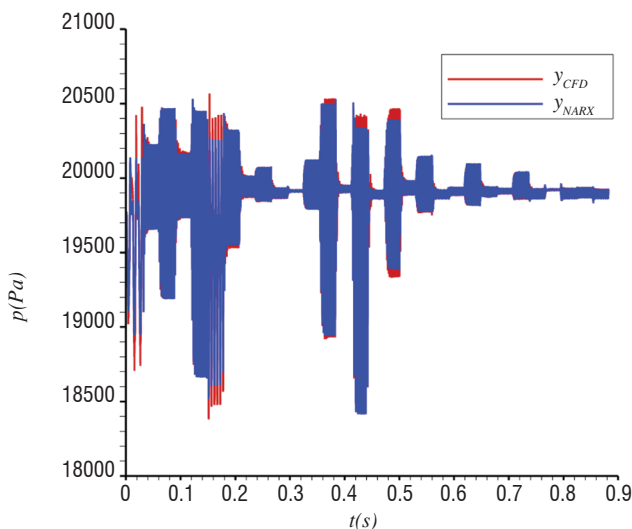
It must be noted that nothing prevents this fit coefficient from being negative.

For the previous set of NARX parameters ($lag_u = 2$, $n_y = 3$, $n_u = 111$ and $p = 5$), a very good fit equal to 84 % is obtained. In comparison, a fit of only 42.7 % is obtained with a linear ARX model with $lag_u = 18$, $n_y = 3$, $n_u = 111$, $p = 1$ and no cross terms giving a total of 115 regressors.

The representations of the response signal computed by the URANS simulation and the signal given by the NARX model for the same identification input command are given in figure 13. This figure shows the ability of the model to represent the temporal pressure evolution of the flow perturbed by the series of forcing frequencies shown in figure 8.

In addition, the black-box model is validated by comparing the model output with CFD results for different forcing frequencies. For each frequency, the measured pressure signal from the URANS simulations is compared with the output of the NARX model for the same input command. Some comparisons are displayed in figure 14. Figure 15 shows the relative error between the model and the CFD results:

$$error(\%)(i) = 100 \times \frac{y_m(i) - y(i)}{y(i)}$$

On the frequency interval covered by the identification command $F^+ \in [0.1; 3]$, the NARX model is in good agreement with the flow computed by URANS simulations. The fit coefficient varies between 48.6 % for the lowest frequency and 93.9 % for the highest. The error between the NARX model and the URANS decreases when the reduced frequency increases and is always lower than 2 % for $F^+ > 0.1$. Outside of this frequency interval (figure 16), the NARX model quickly diverges.

Another important point is to validate the steady state behavior of the NARX model, that is to say, to check whether the mean pressure given by the model is the same as that computed by time-averaging the URANS simulation. The evolution of the time-averaged pressure $<P>$ with respect to the forcing frequency is given in figure 16. On the reduced forcing frequency interval $F^+ \in [0.1; 3]$, mean pressures are in good agreement. Nevertheless, for $F^+ > 3$, the NARX steady pressure estimations quickly diverge from those of the URANS simulation.
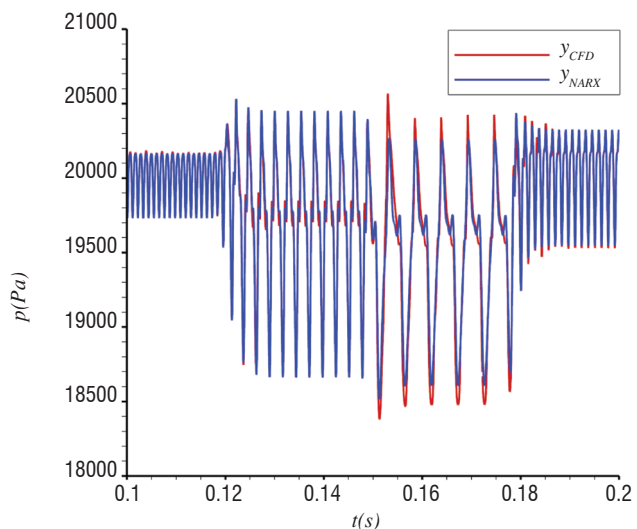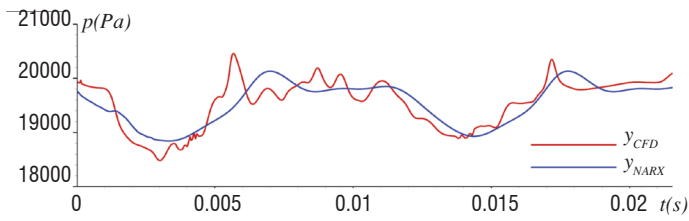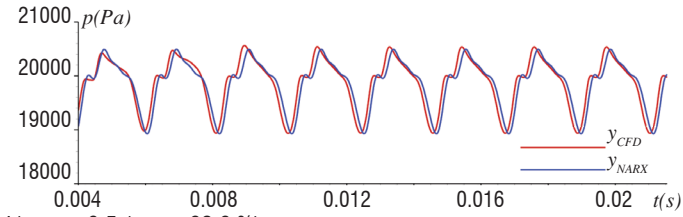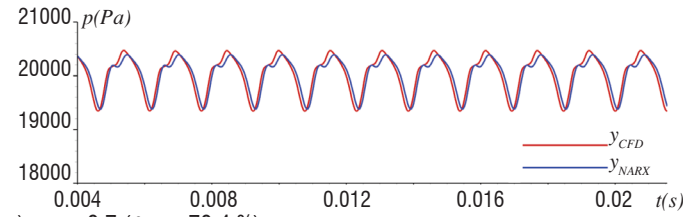

Figure 13 - Comparison of the output of the NARX model (in blue) with the URANS simulation (in red) on the identification signal (left: complete signal, right: zoom for 0.1<t<0.2)
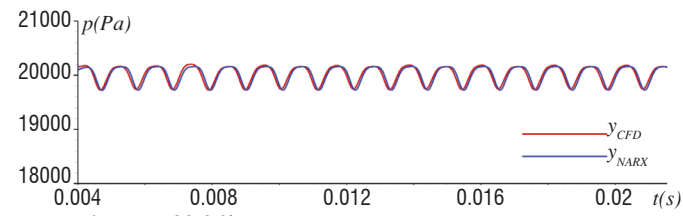
Figure 14 - NARX model validation with open-loop results
for different reduced frequencies
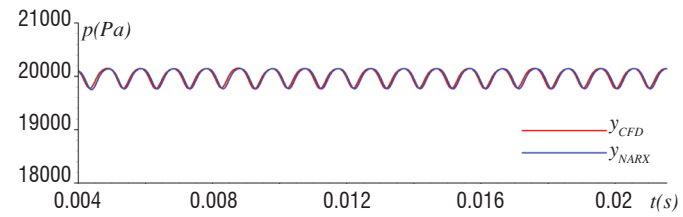
a) $F^+ = 0.1$ (fit = 48.6 %)
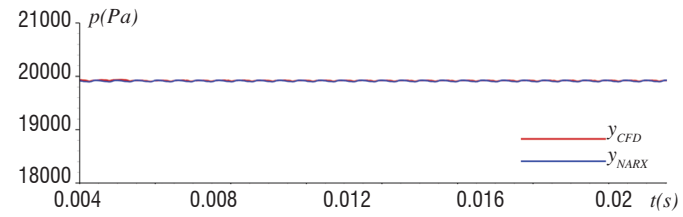
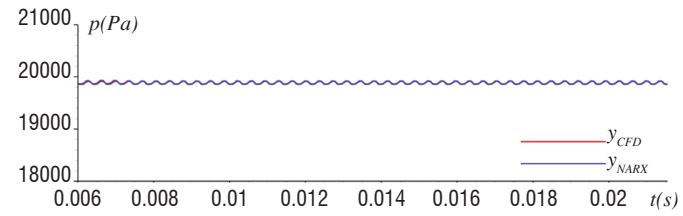b) $F^+ = 0.5$ (fit = 62.6 %)

c) $F^+ = 0.7$ (fit = 70.4 %)

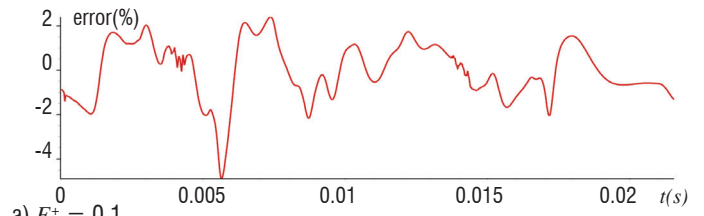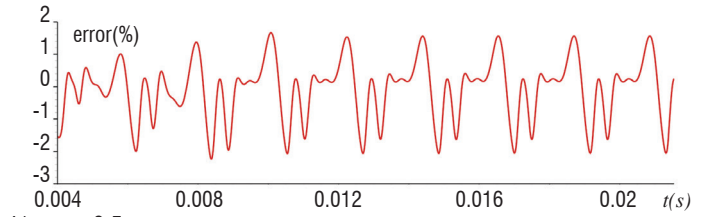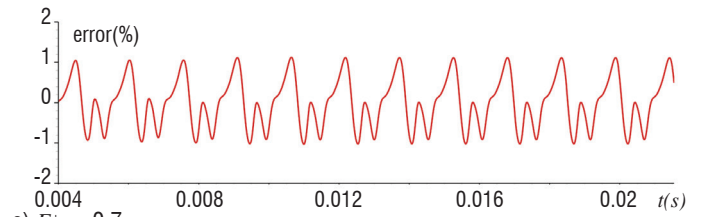d) $F^+ = 1$ (fit = 80.6 %)

e) $F^+ = 1.1$ (fit = 84.8 %)

f) $F^+ = 2$ (fit = 91.9 %)

g) $F^+ = 3$ (fit = 93.9 %)

Figure 15 - Relative error between the NARX model and CFD results
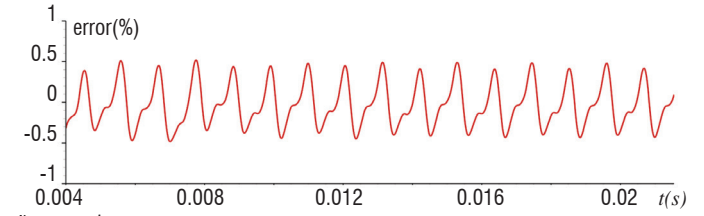for different reduced frequencies
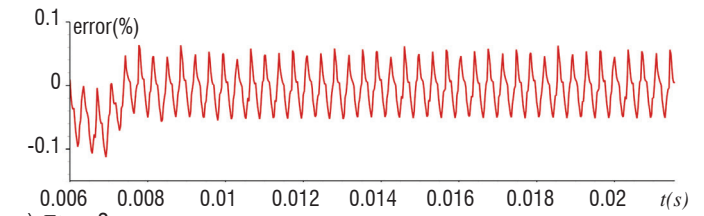
a) $F^+ = 0.1$

b) $F^+ = 0.5$

c) $F^+ = 0.7$

d) $F^+ = 1$

e) $F^+ = 1.1$

f) $F^+ = 2$

g) $F^+ = 3$

As expected, the model can be used for representing the steady pressure frequency response, but only on the frequency bandwidth of the identification signal.
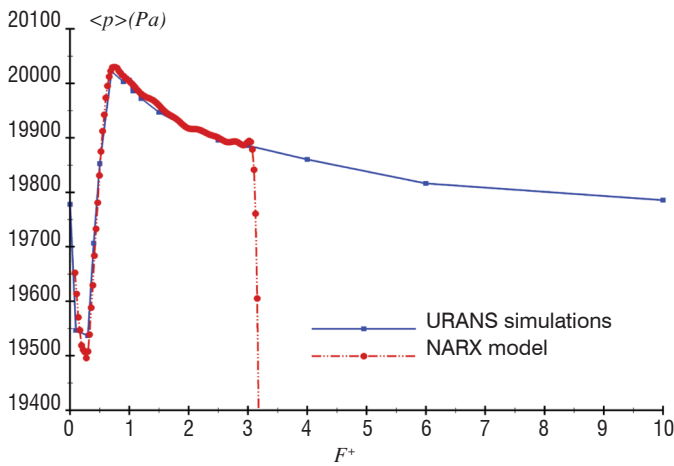

Figure 16 - Comparison of the evolutions of the time-averaged pressure with respect to the forcing frequency between the NARX model (in blue) and the CFD (in red).

Finally, this NARX model is able to accurately represent the steady component as well as the unsteady component of the pressure for $F^+ \in [0.1; 3]$ at the sensor location. The black-box model has its steady maximum at the same frequency as that given by URANS simulations. The NARX reduced-order model can then be used to design a closed-loop algorithm.

Closed-loop control by extremum seeking

Description of the extremum seeking algorithm

The extremum-seeking algorithm is a robust adaptive closed-loop algorithm without an internal model. It is appropriate for the control of nonlinear plants characterized by an output extremum in the steady state. Let a block with a command input u and an output y be a representation of the nonlinear system, with the static input-output-map $y=G(u)$. A typical SISO extremum-seeking structure is given in figure 17.
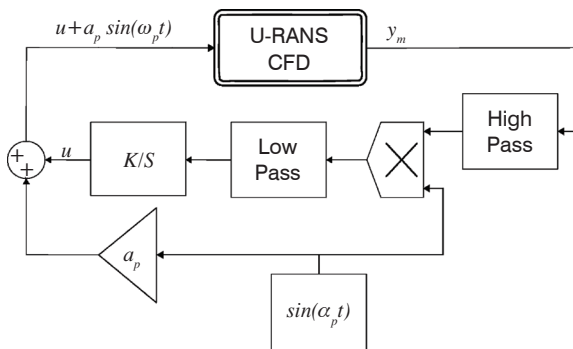

Figure 17 - Block diagram of the basic extremum-seeking feedback algorithm

The extremum-seeking control is based on a gradient online optimization. The aim is to adjust the control input u, in such a way that the maximal steady-state system output $y*$ is achieved without knowing the steady-state input-output map $y=G(u)$ and especially its extremum $y* = max(G(u)) = G(u*)$. The idea is to add a periodic perturbation to the command input u, in order to compute the static input-

output slope and then modify the command u toward the optimal command $u*$.

The perturbation addition is displayed in figure 18, as Step I. Typically, this perturbation is a sine signal $\alpha_p.sin(\omega_p.t)$ where α_p and ω_p denote the perturbation amplitude and pulsation, respectively. The perturbation period must be larger than the largest time constant of the dynamic plant, in order to obtain an approximate sinusoidal output y. If the static input-output slope is positive, then the sinusoidal output and the perturbation are in phase and vice versa (figure 18 Step II). The slope sign is obtained by filtering the system output with a high-pass filter (figure 17: High Pass box) and by demodulating this filtered signal with the perturbation (box with a cross in figure 17). The high-pass filter (Step III in figure 18) removes the mean value and keeps the unsteady component. The demodulation consists in doing the product of the latter with the perturbation signal. Indeed, the product of two signals in phase gives a signal with a positive mean and vice versa (Step IV in figure 18). This demodulation leads to a non-zero mean signal, as long as the maximum is not obtained. This output is passed through a low-pass filter (Low Pass box in figure 17), which gives a moving average value of the slope. The slope sign signal is multiplied by a gain K and integrated (K/s box in figure 17). As a result, the command u is shifted toward the optimal command $u*$, which is displayed in figure 18 as Step V. For more details on the algorithm and in particular a demonstration of the algorithm stability, the reader should consult Ariyur and Krstić [2] and Krstić and Wang [21].
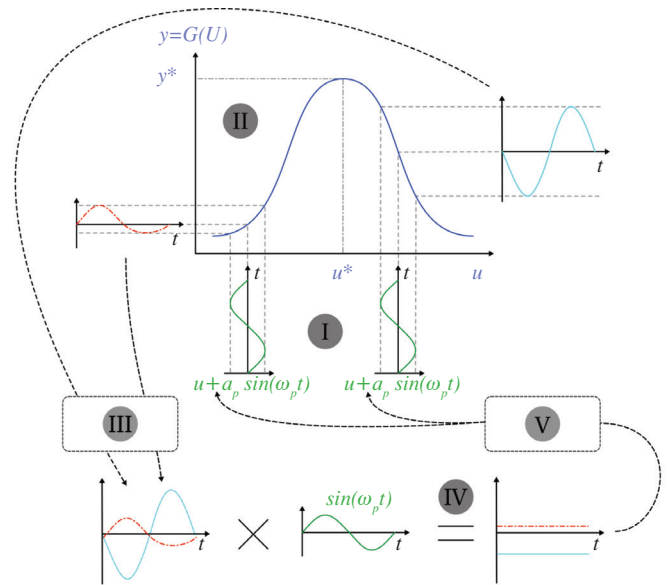
Figure 18 - Extremum-seeking algorithm in 5 steps

Since the extremum-seeking algorithm is based on the slope value estimation using a demodulation step, it is important to use high-pass and low-pass filters with ideal specifications. That is to say, a filter with the shortest possible time response and with a linear phase-shift. The last specification allows a minimum phase distortion, so that different frequencies in the band-pass have the same time delay and the shape of a signal remains unmodified by the filter.

This is the reason why the basic extremum-seeking feedback was improved by using Bessel filters. Bessel filters, also known as Thompson filters, are characterized by an almost constant group

delay across the entire pass-band, thus preserving the wave shape of filtered signals in the pass-band. The "Bessel" approximation aims to develop a normalized low-pass filter, with a maximal constant group delay at the origin. A Bessel low-pass filter is characterized by its transfer function:

$$H(s) = \frac{\theta_n(0)}{\theta_n(s/\omega_0)}$$

where $\theta_n(s)$ are reverse Bessel polynomials and ω_0 is a frequency chosen to give the desired cut-off frequency. The filter has a low-frequency group delay equal to $1/\omega_0$.

The reverse Bessel polynomials are given by:

$$\theta_n(s) = \sum_{k=0}^{n} a_{n|k} s^k \quad \text{with} \quad a_{n|k} = \frac{(2n-k)!}{2^{n-k} k!(n-k)!}$$

Extremum seeking tuning

First, the NARX previously identified in the first part of the paper in the case of flow separation over a ramp is used, with the aim of tuning the parameters of the extremum-seeking algorithm (pulsation ω_p and amplitude α_p of the perturbation, filter cut-off frequencies, loop gain K, etc.) and validating the closed-loop strategy. This NARX black-box model imitates the flow response to a periodic blowing and suction signal. Since the command input given by the extremum-seeking regulator is a frequency, an actuator signal converter is attached to the NARX model for converting the input command to an oscillatory signal. In order to ensure the signal continuity and to introduce actuator dynamics, a first-order transfer function is added to the system model. Its time constant τ allows the time response of the actuator, which is set equal to 0.35 ms here, to be managed.

To tune the extremum-seeking parameters, the U-RANS CFD box in figure 17 is replaced by the NARX model. Thus, the U-RANS CFD box in figure 17 is replaced by the blocks given in figure 19. The moving averaged pressure at the exit of the system block diagram is obtained by filtering the NARX model output with a low-pass filter. A correct mean pressure estimation requires a NARX pressure output averaged over at least two actuation periods. The lower bound of reduced forcing frequency interval is $F^+ = 0.1$, then the mean pressure estimator low-pass filter cut-off frequency ω_m is set equal to $F^+ = 0.05$. A representation of the entire system block diagram is given in figure 19.
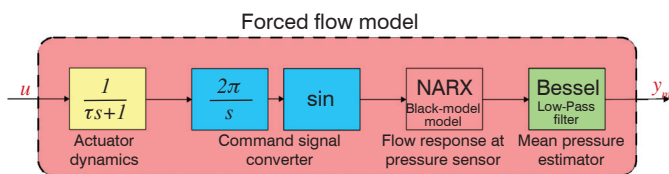

Figure 19 - System block diagram

Concerning the extremum-seeking algorithm itself, there are three pulsations to be chosen: the perturbation pulsation ω_p and the low-pass and high-pass filter ones, ω_{LPes} and ω_{HPes} respectively. The largest time constant of the system is given by the mean pressure estimator low-pass filter cut-off frequency ω_m. Then, it allows the sine perturbation pulsation ω_p to be adjusted. A pulsation ω_p equal to a quarter of ω_m is chosen. The extremum-seeking high-pass filter must remove frequencies larger than ω_p and the direct component. Bessel filters allow a constant group delay, but with a soft magnitude filtering, to be ensured. As a result, ω_{HPes} is set equal to ω_p. The extremum-

seeking low-pass filter must be able to give a moving-average of the slope sign to the integrator. As a mean pressure estimator, the cut-off frequency is adjusted, so that the slope sign signal is averaged over two perturbation periods. Therefore, ω_{LPes} is chosen to be equal to $F^+ = 0.00625$.

Concerning the closed-loop gain K in figure 17, it is in principle a constant; however, here we propose an adaptive gain to increase the convergence rate of the closed-loop. When the steady state map slope is small (at the beginning of the closed-loop), K will be high to increase the convergence rate and, when the slope is large, K will be small to prevent the closed-loop from overshooting and oscillating around the extremum. The expression below has been chosen for the adaptive gain:

$$K(t) = \min\left(K_{max}, \sigma \frac{2a_p \omega_p}{\pi y_{slope}(t)} \right)$$

where K_{max} is a user defined gain and σ is a safety margin with $0 \leq \sigma \leq 1$.

Validation of the extremum seeking parameter choice on the black-box model

Before applying this closed-loop algorithm in an unsteady RANS simulation, it is necessary to validate it on the NARX reduced-order model. The controller is tested in various cases listed in Table 1, where u_0 is an initial forcing frequency. The constant σ is set to be equal to 0.9. Simulations with the NARX model are plotted in figure 20, in which the closed-loop is initiated at $t = 0.1\ s$.

Case	K_{max}	$\alpha_p(F^+)$	$f_p(F^+)$	$u_0(F^+)$
I	1000	0.01	0.0125	0.22
II	1000	0.03	0.0125	0.2
III	1500	0.02	0.0125	1.1

Table 1 - Closed-loop strategy validation cases

For each case, the command converges as expected toward F^+ equal to 0.78. The convergence time depends on the starting frequency point, the maximal gain chosen and the perturbation amplitude value. The representation of the mean pressure at the output of the model is given in figure 21. The extremum-seeking allows the mean pressure maximum that validates the closed-loop strategy to be found.
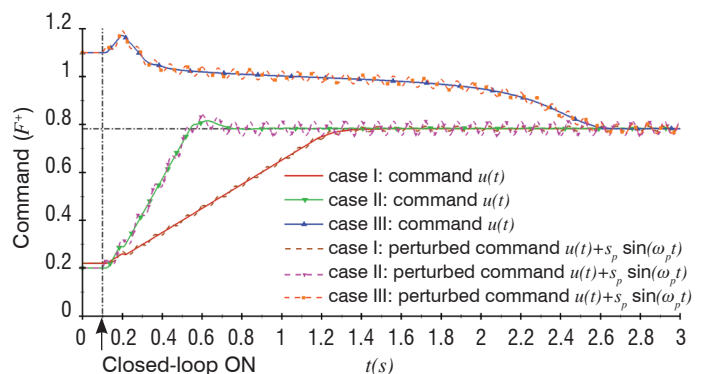

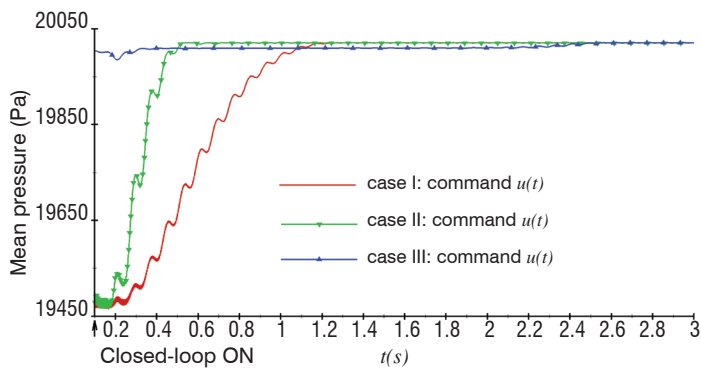Figure 20 - Extremum-seeking with adaptive gain control of the NARX model

Figure 21 - Mean pressure given by the flow model for validation closed-loop

Figure 23 - Moving average pressure from unsteady RANS computations in closed-loop

The closed-loop shows its ability to find in-line the maximum of a nonlinear model. The convergence time is small enough to allow the application of this closed-loop strategy in-line with an unsteady RANS simulation.

Application of the extremum seeking to an URANS computation

After having successfully applied and validated the extremum-seeking controller, the NARX model is replaced by unsteady RANS computations. The controller is tested in the different cases listed in Table 2. The command and mean pressure results are plotted in figure 22 and figure 23, respectively.

Case	K_{max}	$\alpha_p(F^+)$	$f_p(F^+)$	$u_0(F^+)$
I	1000	0.022	0.0125	0.11
II	1000	0.01	0.0125	0.22
III	900	0.03	0.0125	0.2

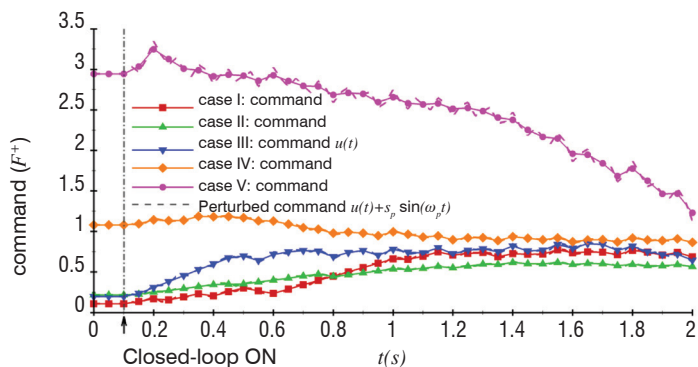Table 2 - Closed-loop in unsteady RANS computation cases

Figure 22 - Extremum-seeking with adaptive gain control of unsteady RANS computations

The convergence time is longer than with the black box model, due to the fact that the model does not perfectly reproduce the true CFD results. Thanks to the robustness of extremum-seeking, the closed-loop is still efficient and the pressure is well maximized. For Cases II, IV and V, simulation must be continued, in order to ensure the frequency command convergence. Cases I and II have converging commands, as expected in the vicinity of F^+ equal to 0.78.
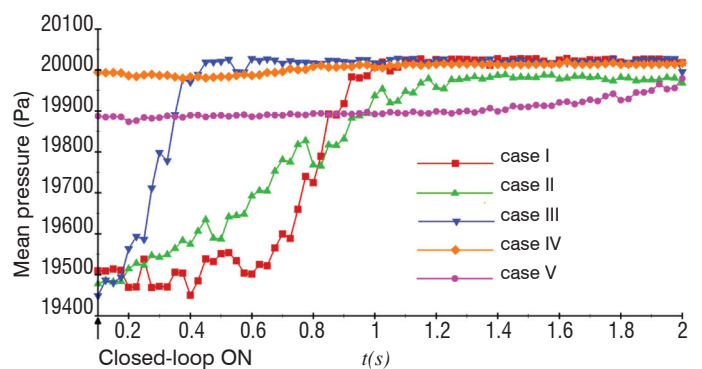
Conclusion

This paper describes a successful approach of closed-loop separation control by synthetic jet on a generic rounded step configuration.

An open-loop study of the forcing frequency has allowed the verification of the system controllability. The chosen objective criterion to be optimized is the mean recirculation bubble surface. The mean wall pressure analysis has shown that maximizing the wall pressure sensor at x/h equal to 2.71 enables the recirculation bubble surface to be minimized.

Maximizing the mean pressure automatically at the sensor location implies the use of a closed-loop algorithm. In a first step, a single-input single-output black-box model was identified, in order to tune and validate the closed-loop strategy. A NARX model of the real time wall pressure signal response to the synthetic jet forcing was successfully designed and validated.

The selected control algorithm was the extremum-seeking, which is a robust adaptive command without internal model. It is appropriate for the control of non-linear plants, characterized by an output extremum in the steady state. The algorithm was improved with an adaptive gain, which guarantees optimal performance in terms of gradient estimation and, with the use of low-pass and high-pass Bessel filters, allows an accurate gradient estimation to be ensured.

The tuning of the control algorithm parameters was based on physical considerations and was validated using the black-box model. The results showed that it was possible to apply this closed-loop strategy in-line with an unsteady RANS simulation.

This control goal was to minimize the recirculation bubble surface. It is also possible, with the same methodology, to control some other criteria, such as the pressure drag or the turbulence level.

Extremum-seeking works with the steady state of the plant, which imposes an estimation of the moving-average state of the output. A simpler black-box model based on the steady state could have been used, but the system dynamics would have been lost.

A next step could be the automatic simultaneous adaptation of frequency and amplitude, using a multi-input multi-output regulator ◼

Acknowledgements

References

[1] H. AKAIKE - *A New Look at the Statistical Model Identification*. IEEE Transactions on Automatic Control. 19(6):716–723 (1974).

[2] K.B. ARIYUR, M. KRSTIĆ - *Real-Time Optimization by Extremum-Seeking Control.* John Wiley & Sons (2003).

[3] A. BANASZUK, S. NARAYANAN, Y. ZHANG -*Adaptive Control of Flow Separation in a Planar Diffuser.* AIAA 41st Aerospace Sciences meeting and Exhibit, AIAA Paper 2003-0617 (2003).

[4] J.F. BEAUDOIN, O. CADOT, J.L. AIDER, J.E. WESFREID - *Bluff-Body Drag Reduction by Extremum-Seeking Control.* J. Fluid and Structure 22(7-8):973-978 (2006).

[5] R. BECKER, R. KING, R. PETZ, W. NITSCHE - *Adaptive Closed-Loop Separation Control on a High-Lift Configuration using Extremum Seeking.* AIAA 3rd Flow Control Conference, AIAA Paper 2006-3493 (2006).

[6] R. BECKER, R. KING, R. PETZ, W. NITSCHE - *Adaptive Closed-Loop Separation Control on a High-Lift Configuration Using Extremum Seeking.* AIAA Journal 45(6):1382-1392 (2007).

[7] G.E.P. BOX, G.M. JENKINS - *Time Series Analysis: Forecasting and Control.* Holden Day, San Francisco (1976).

[8] K.P. BURNHAM, D.R. ANDERSON - *Model Selection and Multimodel Inference: a Practical Information-Theoretic Approach.* 2nd ed. Springer-Verlag (2002).

[9] S. CHEN, S. BILLINGS - *Representation of Non-Linear Systems: the NARMAX Model.* International Journal of Control 49(3):1013-1029 (1989).

[10] J. DACLÈS-MARIANI, G.C. ZILLIAC, J.S. CHOW, P. BRADSHAW - *Numerical/Experimental Study of a Wingtip Vortex in the Near Field.* AIAA J. 33(9):1561-1568 (1995).

[11] J. DANDOIS, E. GARNIER, P. SAGAUT P - *Numerical Simulation of Active Separation Control by Synthetic Jet.* J Fluid Mech. 574:25-58 (2007).

[12] S. DECK - *Delayed Detached Eddy Simulation of Self-Sustained Unsteadiness and Side-Loads in an Overexpanded Nozzle Flow.* Shock Waves 19:239–249 (2009).

[13] Q. GALLAS, R. HOLMAN, T. NISHIDA, B. CARROLL, M. SHEPLAK, L. CATTAFESTA - *Lumped Element Modeling of Piezoelectric-Driven Synthetic Jet Actuators.* AIAA J 41(2):240-247 (2003).

[14] Q. GALLAS, G. WANG, M. PAPILA, M. SHELPLAK, L. CATTAFESTA - *Optimization of Synthetic Jet Actuators.* AIAA 41st Aerospace Sciences meeting and Exhibit, AIAA Paper 2003-0635 (2003).

[15] E. GARNIER, P.Y. PAMART, J. DANDOIS, P. SAGAUT - *Evaluation of the Unsteady RANS Capabilities for Separated Flows Control.* Computers & Fluids, 61:39-45 (2012).

[16] C.W. GEAR - *Algorithm 407-DIFSUB for the Solution of Ordinary Differential equations.* Commun. ACM, 14(3):185-190 (1971).

[17] P.C. HANSEN, D.P. O'LEARY - *The Use of the L-curve in the Regularisation of Discrete ill-Posed Problems.* SIAM J. Sci. Comput. 14(6):1487-1503 (1993).

[18] L. HENNING, R. BECKER, G. FEUERBACH, R. MIMINOVIC, R. KING, A. BRUNN, W. NITSCHE - *Extensions of Adaptive Slope-Seeking for Active Flow.* Proceedings of the Institution of Mechanical Engineers, Part I: Journal of Systems and control Engineering, 222:309-322 (2008).

[19] R. HOLMAN, Y. UTTURKAR, R. MITTAL, B.L. SMITH, L. CATTAFESTA - *Formation Oriterion for Synthetic Jets.* AIAA J 43(10):2110-2116 (2005).

[20] R. KING, R. BECKER, M. GARWON, L. HENNING - *Robust and Adaptive Closed-Loop Control of Separated Shear Flows.* AIAA 2nd Flow Control Conference, AIAA Paper 2004-2519 (2004).

[21] M. KRSTIĆ, H.H. WANG - *Stability of Extemum Seeking Feedback for General Nonlinear Dynamic Systems.* Automatica, 36:595-601 (2000).

[22] I. MARY, P. SAGAUT - *Large Eddy Simulation of a Flow Around an Airfoil Near Stall.* AIAA J 40(6):1139-1145 (2002).

[23] J. NEUMANN, H. WENGLE - *Coherent Structures in Controlled Separated Flow over Sharp-Edged and Rounded Steps.* J Turb 5:1-24 (2004).

[24] P.Y. PAMART, J. DANDOIS, E. GARNIER, P. SAGAUT - *Large Eddy Simulation study of Synthetic Jet Frequency and Amplitude Effects on a Rounded Step Separated Flow.* 5th AIAA Flow Control Conference, AIAA Paper 2010-5086 (2010).

[25] M. PAMIÈS, E. GARNIER, A. MERLEN, P. SAGAUT - *Response of a Spatially Developing Turbulent Boundary Layer to Active Control Strategies in the Framework of Opposition Control.* Phys. Fluids 19:108102 (2007).

[26] M. PASTOOR, L. HENNING, B.R. NOACK, R. KING, G. TADMOR - *Feedback Shear Layer Control for Bluff Body Drag Reduction.* J. Fluid Mech. 608:161-96 (2008).

[27] J. RIOU, E. GARNIER, C. BASDEVANT - *Compressibility Effects on the Vortical Flows Over a 65 deg Sweep Wing.* Phys. Fluids 22:035102 (2010).

28. J.M. SCHUSTER, D.R. SMITH - *A Study of the Formation and Scaling of a Synthetic Jet.* 42nd AIAA Aerospace Sciences Meeting and Exhibit. AIAA Paper 2004-90 (2004).

[29] A. SEIFERT, L.G. PACK - *Oscillatory Excitation of Unsteady Compressible Flows over Airfoils at Flight Reynolds Number*, AIAA Paper 99-0925 (1999).

[30] A. SEIFERT, T.BACHAR, D. KOSS, M. SHEPSHELOVICH, I. WYGNANSKI - *Oscillatory Blowing: a Tool to Delay Boundary-Layer Separation.* AIAA J. 31(11):2052-2060 (1993).

[31] P.R. SPALART, S.R. ALLMARAS - *A One Equation Turbulence Model for Aerodynamics Flows.* 30th AIAA Aerospace Sciences meeting and Exhibit, AIAA Paper 1992-0439 (1992).

[32] A.N. TIKHONOV, V.A. ARSENIN - *Solution of ill-Posed Problems.* Winston & Sons, Washington (1977).

[33] S. TRAPIER, S. DECK, P. DUVEAU - *Delayed Detached Eddy Simulation and Analysis of Supersonic Inlet Buzz.* AIAA J. 46(1):118–131 (2008).

Acronyms

SISO	(Single-Input Single-Output)	MA	(Moving Average model)
NARX	(Nonlinear Auto-Regressive with eXogenous input)	ACF	(Auto-Correlation Function)
NARMAX	(Nonlinear Auto-Regressive Moving Average with eXogenous input)	PACF	(Partial Auto-Correlation Function)
		AIC	(Akaike Infomation Criterion)
RANS	(Reynolds Averaged Navier-Stokes)	RSS	(Residual Sum of Squares)
LES	(Large-Eddy Simulation)	CFD	(Computational Fluid Dynamics)
AR	(Auto-Regressive model)		

AUTHORS

Julien Dandois graduated from the Ecole Nationale Supérieure d'Arts et Métiers (ENSAM) in 2003 and received a PhD in Fluid Mechanics from Paris 6 University in 2007. Since that time, he has worked in the Civil Aircraft Unit of the Applied Aerodynamics Department, in the fields of high-lift, separation control, buffet control, closed-loop control and aeroacoustics.

Pierre-Yves Pamart graduated from ISAE-ENSMA in 2007. He received a PhD in Fluid Mechanics from Paris 6 University in 2011. The subject of his thesis was the closed-loop control of a separation. Then, he became a research engineer in aerothermal methods and HVAC in the building field at CSTB. In 2012, he joined SAFRAN-Snecma, in the aerothermal and multi-physics methods department.